Renewable Energy 108 (2017) 380–389

Contents lists available at ScienceDirect

Renewable Energy

journal homepage: www.elsevier.com/locate/renene

Dynamic rating of overhead transmission lines over complex terrain using a large-eddy simulation paradigm

Tyler Phillips [a], Rey DeLeon [a, b], Inanc Senocak [a, *]

[a] Department of Mechanical & Biomedical Engineering, Boise State University, Boise, ID, 83725, United States
[b] Department of Mechanical Engineering, University of Idaho, Moscow, ID, 83844, United States

ARTICLE INFO

Article history:
Received 1 October 2016
Received in revised form
21 February 2017
Accepted 24 February 2017
Available online 27 February 2017

Keywords:
Computational fluid dynamics
Dynamic line rating
Wind power

ABSTRACT

Dynamic Line Rating (DLR) enables rating of power line conductors using real-time weather conditions. Conductors are typically operated based on a conservative static rating that assumes worst case weather conditions to avoid line sagging to unsafe levels. Static ratings can cause unnecessary congestion on transmission lines. To address this potential issue, a simulation-based dynamic line rating approach is applied to an area with moderately complex terrain. A micro-scale wind solver — accelerated on multiple graphics processing units (GPUs) — is deployed to compute wind speed and direction in the vicinity of powerlines. The wind solver adopts the large-eddy simulation technique and the immersed boundary method with fine spatial resolutions to improve the accuracy of wind field predictions. Statistical analysis of simulated winds compare favorably against wind data collected at multiple weather stations across the testbed area. The simulation data is then used to compute excess transmission capacity that may not be utilized because of a static rating practice. Our results show that the present multi-GPU accelerated simulation-based approach — supported with transient calculation of conductor temperature with high-order schemes — could be used as a non-intrusive smart-grid technology to increase transmission capacity on existing lines.

1. Introduction

Investments in renewable energy has been driven by several factors, including energy security and stability, climate change, and economics. Since 2000, wind energy has been the largest source of new renewable generation installed in the United States [1]. However, wind power generation is much more complex than installing wind turbines in windy areas. Grid integration is a major challenge, many of the best locations for wind farms do not have access to the needed transmission capacity [2]. Congestion in existing transmission lines is a growing concern, resulting in inefficiencies for both renewable energy producers, utilities and balancing authorities [3]. At times, transmission service providers (TSPs) may not be able to absorb the power generated, therefore, power production can be curtailed.

Potential sites for wind power generation are usually found in remote open areas that are away from populated cities, where electricity is needed most. Historically, transmission systems have been built together with power production installations in order to meet the electricity demand. For economic reasons they are usually not over-sized, therefore, current transmission networks in many of these sites may not support additional generation. Many wind projects have been able to patch into the existing transmission network, however, these opportunities are shrinking. Further expansion of wind energy may require large investments in transmission networks, creating an obstacle for cost-effective wind deployment [1,4].

Transmission capacity can be increased in several ways. The obvious way is to reinforce the transmission network with new powerlines. However, this is constrained by the high costs and legal challenges of building new powerlines [5]. Therefore, TSPs have focused on innovative solutions that modifies existing network to increase transmission capacity. Different techniques include prediction of meteorological conditions by means of deterministic [6] or probabilistic [7] forecasting methods, and adopting the newest innovations in smart-grid real-time monitoring of temperature, sag, tilt, power, current and weather conditions [8–10]. In the case of wind energy integration, monitoring meteorological conditions in real-time can be very beneficial for both power generation and

* Corresponding author.
E-mail address: senocak@boisestate.edu (I. Senocak).

http://dx.doi.org/10.1016/j.renene.2017.02.072
0960-1481/

transmission purposes. Strong winds needed for wind generation, will also cool down the conductor of local transmission lines, creating additional capacity, which would enable TSPs to "overload" the line when it is needed most [11,12].

Transmission conductor capacity is limited by its maximum allowable temperature. The maximum amount of electric current a conductor can transmit before structural damage is known as *ampacity*. Currently, ampacity is generally determined using a static line rating (SLR) methodology. SLR is based on conservative assumptions regarding environmental conditions, such as high ambient temperature and low wind conditions. These assumptions were made to avoid lines sagging to unsafe levels. However, they are overly conservative for areas where wind generation is abundant. Therefore, TSPs are investigating dynamic line rating (DLR) methods to increase ampacity on existing lines. DLR utilizes real-time environmental conditions to better predict the temperature of the conductor. Deployment of DLR has the potential to reduce the estimated $60 billion needed in transmission infrastructure to meet the 20% wind energy by 2030 [2].

Fernandez et al. [13] provide a comprehensive review of real-time DLR technologies that have been developed over the last 30 years, endorsing the potential of DLR for wind power integration. Commercially available DLR technologies include direct line sag, line tension, and conductor temperature measurements [14]. Wind turbines are increasingly being built in areas of complex terrain, as available sites on flat terrain is diminishing. In complex terrain elevated positions like hill tops are favorable sites due to the increased wind speed. However, complex terrain proves to be challenging for the aforementioned DLR systems. Sag and tension monitoring systems can only inform TSPs of the average sag or tension measurement over large sectionalized transmission spans, therefore, only the average temperature of the conductor over large sections can be known. Direct temperature measurements at a single location may not necessarily represent the critical span, or the hottest section along a conductor. Studies have shown that conductor temperature can vary spatially by 10–20 °C due to variations in wind speed and direction [15–17]. Therefore, currently adopted DLR systems may not be a good solution for determining the real-time transmission capacity in regions of complex terrain. If implemented, they may potentially lead to severe overestimation of the actual ratings, allowing the conductor to be overloaded and causing degradation of the line. Adding more monitoring devices could be a solution, however these systems are typically expensive for wide deployment that is needed to reduce risks to an acceptable level [18]. Additionally, implementation of direct DLR systems can prove to be challenging, as transmission lines need to be de-energized during installation and regular maintenance. Therefore, a non-intrusive DLR solution is highly desirable, which also motivates the present study.

In Greenwood et al. [19] two non-intrusive approaches were compared. One approach adopted a CFD-based library approach to extract wind speeds and direction along the path of transmission lines and the other approach used an uncertainty model based on a small number of weather stations. Greenwood et al. suggested that a more sophisticated wind model that can accurately capture the time-dependent nature of winds over complex terrain coupled with uncertainty quantification would be invaluable to expand the DLR concept. Michiorri et al. [20] used actual environmental conditions from a limited number of meteorological stations as input to the steady-state thermal models. An inverse distance interpolation technique and a power law for wind profile were used to estimate the environmental conditions at transmission line. A state-estimation algorithm based on the Monte-Carlo approach was then used to take into account the uncertainty in data. Michiorri et al. identified the source of errors as the physical models used in their approach, and suggested the use of wind flow models based on the computational fluid dynamics (CFD) approach.

With today's improved wind and weather modeling and high performance computing capabilities, the use of computer simulations to forecast wind and determine transmission capacity has emerged as an alternative to intrusive hardware solutions. Short-term wind forecasting can potentially be a valuable tool for TSPs, enabling conductor temperature calculations at dense intervals along transmission lines in complex terrain. Michiorri et al. [21] reviewed current meteorological forecasting technologies for broadening the adoption of DLR and particularly drew attention to the current need to improve low wind speed modeling and turbulence. Michiorri et al. promote the viewpoint of moving from monitoring technologies to an active management technology where wind forecasting for different time horizons becomes critical. To this end, our large-eddy simulation approach directly addresses the need to improve low wind speed modeling in the vicinity of transmission lines.

Meso-scale numerical weather prediction models have long been used to forecast winds and other meteorological variables, however their application to micro-scale atmospheric boundary layer flows over complex terrain with a horizontal spatial resolution ranging from 10 to 100 m is still an on-going research and far from realizing the forecasting mode. Mesoscale weather forecasting models typically adopt spatial resolutions on the order of a few kilometers. Results from existing foresting models vary greatly depending on the locations and time period investigated [22–26]. On relatively flat terrain use of mesoscale models may prove effective, but fine-scale forecasting solutions that can resolve complex terrain features with horizontal resolution on the order of 10 m are needed. For instance micro-scale complex terrain forecasting models could be used to quantify the stochastic variations in line ratings, which could then be converted to dynamic constraints as described by Banerjee et al. [27].

In what follows, we present the equations for dynamic line rating, followed by our massively-parallel, micro-scale wind solver to predict wind speed and direction as a function of time. An actual test area with moderately complex terrain is simulated, and predictions are compared against available weather station data at multiple locations. Field and simulation data are then used to compute available ampacity for a dynamic line rating scenario, demonstrating the potential of the current non-intrusive approach to increase transmission capacity.

2. IEEE standard 738-2012 transmission capacity calculation

Transmission line capacity is commonly calculated using procedures described either in the Institute of Electrical and Electronics Engineers (IEEE) 738 Standard [28] or the CIGRE Standard [29]. In this study, we follow the IEEE standard and describe the salient features of the calculation procedure for clarity.

Temperature of an overhead electrical conductor is a function of its material properties, weather conditions, and electrical current. The steady-state heat balance is given as

$$q_c + q_r = q_s + q_j, \tag{1}$$

where q_c, q_r, q_s, and q_j are the conductor convective heat loss, radiated heat loss, solar heat gain, and Joule heating, respectively.

Joule heating is calculated using the electric current, I, and conductor resistance, $R(T_{ave})$, which is a function of its average temperature, T_{ave}. Joule heating is given as

$$q_j = I^2 \cdot R(T_{ave}). \tag{2}$$

The steady-state thermal rating used to calculate conductor capacity is then expressed as

$$I = \sqrt{\frac{q_c + q_r - q_s}{R(T_{ave})}}, \tag{3}$$

where resistance is determined at the maximum permissible conductor temperature from lookup tables. It is common practice to use this equation under conservative assumptions for weather conditions, especially for convective heat loss, to rate transmission lines. This practice, known as the *static line rating*, often leads to stringent limits, not enabling the real-time capacity of the line to be utilized.

2.1. Dynamic ratings

The steady-state rating given in Eq. (3), is calculated using conservative estimates of weather conditions. CIGRE [30] recommends that base ratings should be calculated with an effective wind speed of 0.6 m/s, an air temperature near the seasonal maximum (40 °C summer) and a solar radiation of 1000 W/m^2. In reality the electrical current through the conductor and real-time weather conditions exposed to the line are constantly changing. In response to these changes, conductor temperature varies with an associated time scale. Since the temperature of the conductor is what limits its capacity, we want to track its temperature in real-time. The change in temperature from an increase in current from 800 to 1200 and 1300 Amps is shown by the digitized data [28] in Fig. 1.

Transient response of a conductor's temperature to changing current and weather conditions can be modeled as a first-order ordinary differential equation (ODE) expressed as

$$\frac{dT_{ave}}{dt} = \frac{1}{mC_p}\left[q_j + q_s - q_c - q_r\right], \tag{4}$$

where mC_p is the total heat capacity of the conductor, given as

$$mC_p = \sum m_i C_{pi}, \tag{5}$$

where m_i and C_{pi} are the mass per unit length of i^{th} conductor material and the specific heat of i^{th} conductor material, respectively. Therefore, if the electrical current and real-time conditions are known, the ODE can be solved numerically to calculate real-time temperature of the conductor. With the use of a wind forecasting model, conductor temperature can not only be potentially forecast, but it can be done at very dense intervals, which may not be feasible with current hardware solutions. This would give TSPs an unprecedented understanding of the current and future state of the transmission lines, allowing for better efficiency of the transmission and generation network.

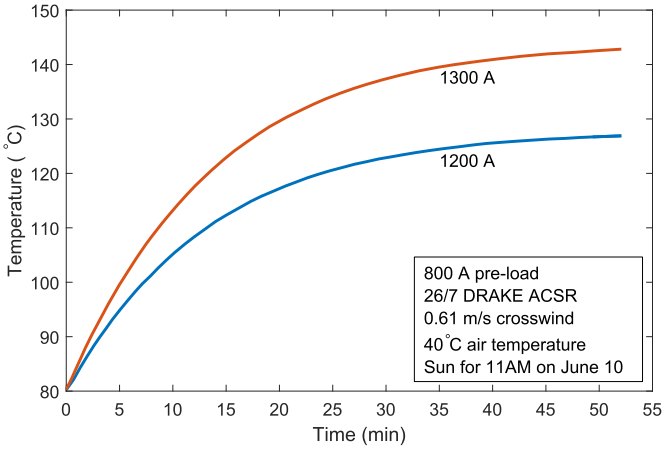

Fig. 1. Transient temperature response to a step change in current from 800 to 1200/1300 Amps. Graph adapted from Ref. [28].

The ODE given in Eq. (4) represents an initial value problem (IVP). The general form is expressed as

$$\frac{dy}{dt} = f(t, y) \tag{6}$$

over a time interval

$$a \le t \le b \tag{7}$$

subject to an initial condition

$$y(a) = y_0. \tag{8}$$

The IEEE Standard 738-2012 does not give a recommended numerical method to solve the ODE given in Eq. (4). However, it does supply a sample computer code as a convenience to the user. In that sample code, a first-order accurate forward Euler method is used. In the standard, it is also pointed out that other numerical methods may well be more appropriate in certain situations. Additionally, it is noted that time step size be kept small to reduce numerical errors.

We believe a forward Euler method is too crude for a critical system such as transmission lines. Therefore we examine the use of a fourth-order accurate Runge-Kutta (RK4) scheme [31] for improved accuracy and computation time. The IEEE standard states that there seems to be little advantage in using a time step greater than 1 s. This may be true when doing a single transient temperature calculation for demonstration purposes, as done in the IEEE standard. However, we are interested in implementing a real-time dynamic rating in practice, which will likely require many thousands of these calculations to be performed along the length of transmission lines. Therefore, computational expense may become an issue when using a forward Euler method with small time steps. An RK4 scheme allow us to assume larger time step sizes while keeping the error low.

An RK scheme can be written as

$$y_{i+1} = y_i + \phi(t_i, y_i, h)\cdot h, \tag{9}$$

where $\phi(t_i, y_i, h)$ is called the increment function, which is a representative slope over the interval h. The following 4^{th} order RK scheme (RK4) is used in this study.

$$y_{i+1} = y_i + \frac{1}{6}(k_1 + 2k_2 + 2k_3 + k_4)\cdot h, \tag{10}$$

where k's represent slope estimates.

As a test case to compare both numerical methods, we have performed the same 800 to 1200 step increase in current provided in the IEEE 738 Standard, shown in Fig. 1. A normalized L2-norm is used to quantify the difference between the two methods. The normalized L2-norm is given by

$$\|x\| = \frac{1}{N}\sqrt{x_i^2}, \tag{11}$$

where N is the number of comparisons between the exact and numerical solution and x_i is the difference between them. There is no analytical solution, therefore, a reference value was used as the exact solution. The exact value was calculated using the RK4 method and a time step of 0.01 s.

The results are shown in Fig. 2, and tabulated in Table 1. This test case makes it clear that care needs to be taken with the selection of a numerical method, the resulting conductor temperature and computation time can be greatly affected. If a DLR system is put in place, it is critically important that temperature computations can be completed in near real-time while keeping numerical errors to an acceptable level. Using the RK4 method allows a time step size of 300s over the Euler of 1s, while keeping numerical errors at the same order of magnitude. This allows calculations to be completed over 90 times faster, potentially reducing computation time from minutes to seconds. This time could prove critical for TSP, giving them additional time to make needed transmission decisions. Therefore, we recommend an RK4 scheme for calculating the temperature of a conductor as it is easy to implement and there is a clear benefit to it.

Table 1
Normalized L2-norm of conductor temperature using a forward Euler and 4^{th} order Runge-Kutta method. The "exact" values are calculated using the RK4 and a time step (dt) of 0.01s. The speedup is based of the Euler calculation with a time step of 1s.

dt(s)	L2-norm		Speedup	
	RK4	Euler	RK4	Euler
1	1.8E-14	1.1E-4	0.3	1
10	9.4E-11	3.4E-3	3.0	10
30	1.3E-8	1.8E-2	9.2	31
60	3.1E-7	5.0E-2	19	61
300	5.1E-4	0.58	93	314
600	1.4E-2	1.8	186	616
1200	0.52	7.5	367	1266

3. Massively-parallel wind solver

The need for accurate wind modeling, especially at low speeds and over complex terrain, were mentioned in recent studies [13,21]. Steady-state CFD solutions based on Reynolds-averaged Navier-Stokes (RANS) equations may not capture the unsteady nature of winds over complex terrain. The large-eddy simulation technique (LES) is inherently unsteady and generally produces better results for separated flows over complex terrain. However, LES is expensive in terms of computational resources, because fine spatial resolutions are needed to resolve energetic eddies. On the other hand, fine resolutions could be beneficial to better monitor the conductor temperature along its path. The unsteady nature of the wind simulations could also help capture the transient response of the conductor to establish a reliable line rating technique. To this end, advances in parallel computing technology can help broaden the adoption of LES technique in practical problems. Graphics processing units offer a relatively economical solution as a small-footprint computing platform because of their massively parallel architecture.

In this study, we adopt a multi-graphics-processing-unit-accelerated (multi-GPU), parallel wind solver, GIN3D [32–36], as an improved solution for wind modeling over complex terrain. Depending on the mesh size, GIN3D has the potential to compute winds over arbitrarily complex terrain faster than real-time. Computational domain size can range from meters to several kilometers. The computations are accelerated on GPU clusters with a

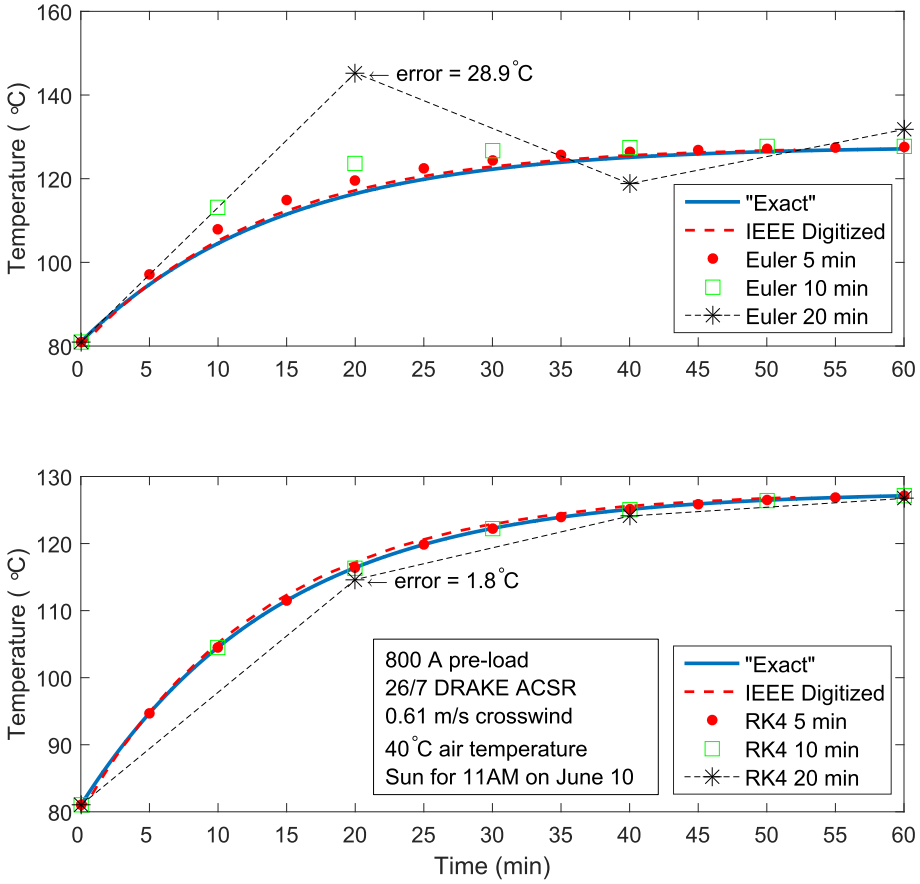

Fig. 2. Transient conductor temperature solution using a forward Euler method (top) and a 4^{th} order Runge-Kutta method (bottom) with time steps of 5, 10, and 20 min. The "Exact" value was calculated using the RK4 and a time step of 0.01s. IEEE standard solution has been digitized.

dual-level parallel implementation that interleaves Message Passing Interface (MPI) with NVIDIA's Compute Unified Device Architecture (CUDA). For instance, an area of approximately 6.5 km by 5.7 km with a spatial resolution of 15 m in the horizontal and 8 m in the vertical, simulations can be 2.2. times faster than real-time on 4 T K20 GPUs. In this study, we will execute GIN3D by imposing a wind direction inferred from local measurements to assess potential of a simulation-based DLR approach. Our future goal is to forecast micro-scale atmospheric flows over complex terrain with a model-chain approach where lateral boundary conditions are informed by a mesoscale weather forecasting model.

The large-eddy simulation (LES) technique is used in GIN3D for subgrid-scale turbulence closure. In LES of atmospheric flows, it is common practice to employ a wall-model due to the complexity and roughness of terrain and the inadequate resolution in the vicinity of the surface. In particular we pursue a hybrid Reynolds-averaged Navier-Stokes (RANS) LES technique. We employ the hybrid eddy viscosity model proposed in Ref. [37] which can be written as follows,

$$\nu_t = \left[([1-\exp(-z/h_{RL})]C_S\Delta)^2 + (\exp(-z/h_{RL})\kappa z)^2\right]\left|\bar{S}\right|, \qquad (12)$$

where z is the surface-normal distance, h_{RL} is the RANS-LES transition height, $C_S\Delta$ representing the sub-grid-scale (SGS) mixing length (C_S being the model coefficient and Δ the LES filter width), and κz representing the RANS mixing length. The SGS mixing length is determined using the Lagrangian dynamic SGS methodology [38] applied to the Smagorinsky eddy viscosity model. The Lagrangian dynamic model is a localized SGS model that does not require any homogeneous directions in the computational domain. Therefore, it is adequate for arbitrarily complex terrain. The RANS mixing length is that of Prandtl [39].

We prefer a Cartesian method to solve the governing equations as it maps well to the computer architecture of modern GPUs. The immersed boundary (IB) method is used to impose boundary conditions on the surface using logarithmic reconstructions [40] in conjunction with the above hybrid eddy viscosity model. Note that the goal is to produce the correct Reynolds stresses at the surface. Therefore, it is important that the velocity reconstruction scheme is consistent with eddy viscosity near the surface. A logarithmic reconstruction therefore is suitable because it is consistent with the Prandtl's mixing length model near the surface.

While IB methods eliminate cumbersome meshing and poor mesh quality (e.g. skewed cells), the challenge is to impose the boundary conditions as the immersed surface will most likely not coincide with the Cartesian grid points. We employ the direct-forcing approach proposed by Ref. [41] and later applied by Ref. [42]. This IB method can be classified as a “sharp interface” IB method, as the boundary condition at the surface appears explicitly in the method. The first step of this IB method is to identify the Cartesian grid cells cut by the surface, which can be challenging with arbitrarily complex terrain. The details of the geometric pre-processing can be found in Ref. [43]. Once the geometric information is known, the values in near-surface grid cells cut by the immersed surface can be reconstructed each simulation time step by interpolating between the known boundary condition at the immersed surface, e.g. the no-slip condition for velocity, and resolved values from the flow field where the grid cells are not cut by the immersed surface. The logarithmic reconstruction scheme for velocity proposed by Ref. [40] is revised to explicitly enforce the impermeability condition over complex terrain. First, the velocity components are projected onto surface-parallel and surface-normal vectors, $u_{i,t}$ and $u_{i,n}$. The reconstruction scheme for the normal components is a linear interpolation between the flow at a sufficient surface-normal distance, z_2, and the no-slip condition at the immersed surface,

$$u_{i,n}\big|_{z_1} = u_{i,n}\big|_{z_2}\frac{z_1}{z_2}, \qquad (13)$$

where z_1 is the IB node wall-normal distance. The impermeability condition is then explicitly enforced. The tangential reconstruction scheme is based on logarithmic-similarity in the atmospheric surface layer [44] and is given by

$$u_{i,t}\big|_{z_1} = u_{i,t}\big|_{z_2}\frac{log(z_1/z_0)}{log(z_2/z_0)}, \qquad (14)$$

using the same surface-normal distances as in Eq. (13), where z_0 is the aerodynamic roughness length.

3.1. Simulation setup

The target computational domain is ~368 km^2 shown in Fig. 3. Periodic boundary conditions were applied in the lateral directions, deemed suitable as the elevation changes relative to the total height of the computational domain are small. As complex terrain may not be the same elevation on all sides of the domain, we extended and tapered the target domain down such that the elevation is constant along the perimeter of the domain. This added approximately 6–7 km to each side. The total domain height is ~2 km from the lowest elevation. The Cartesian grid consisted of ~539 million points, giving lateral resolution of ~30 m and vertical resolution of 4 m. Simulation parameters are given in Table 2.

The wind flow is driven by a constant 6.0e-05 m/s^2 pressure gradient coming from the north-east at an angle of 63.3° using meteorological conventions (i.e. wind coming from north is 0° and clock-wise is positive.). The pressure gradient was adjusted iteratively to approximately match the observed wind speed at a weather station over flat terrain. The top of the domain is set to a free-slip condition. Fluid properties are that of air at standard temperature. Surface roughness, z_0, is set to 0.15 m, a value suggested in Ref. [44] for rural farmland areas. Following [37], the RANS-LES interface, h_{RL}, is set to 31.6 m, twice the size of the LES filter width, $\Delta = \sqrt[3]{\Delta x \Delta y \Delta z}$. The flow is initialized by superimposing high-amplitude, low-frequency sinusoidal perturbations onto a rough-surface log-law profile. This was a necessary step as the terrain elevation changes were not enough to trip turbulence unassisted, a further indication that periodic boundary conditions are suitable for this case. The flow was allowed to develop for 2 h of simulated time before reaching a stationary state. The wind solver

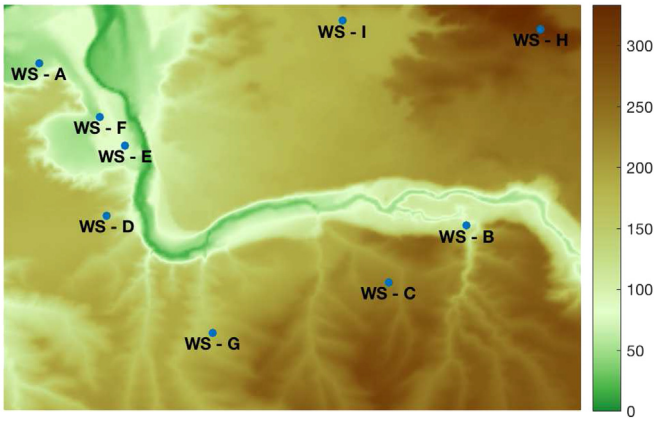

Fig. 3. Section of INL/IPCo test site for DLR research, colored by terrain height.

Table 2
Simulation parameters. Target domain is centered in the total domain which includes the extension and tapering regions for the periodic boundary conditions.

Domain size (km)			Grid Points			Resolution (m)		
L_x	L_y	L_z	N_x	N_y	N_z	Δx	Δy	Δz
16.0	23.0	1.94	1025	1025	513	29.3	34.2	3.9

assumes incompressible flow, solving the Poisson equation with geometric multigrid designed for multi-GPUs [34] and uses second-order central difference schemes for spatial derivatives and a second-order Adams-Bashforth scheme for time integration.

4. DLR test area

Idaho Power Company (IPCo) and Idaho National Laboratory (INL) joint test bed area for DLR research is located on the Snake River Plain in southern Idaho. The test site lies in an area of high desert with complex terrain, covering an area approximately 1,500 km^2 with an elevation range of 754 m to 1,1198 m.

Seventeen weather stations were mounted by IPCo/INL team at a height of 10 m agl in strategic locations along more than 190 km of high-voltage transmission lines. Data collection through a cellular network has been underway by IPCo since August of 2010. The measured quantities are wind speed, wind direction, ambient temperature, and solar irradiation. Data from the weather stations is collected every 3 min, it is an average of 2 s readings over the 3-min time interval. Weather stations use NRG 40C [45] or the APRS #40R [46] three cup anemometers. Both models have similar specifications; wind speed accuracy of 0.1 m/s with a sensor range of 1–96 m/s. In Phillips et al. [47] a year-long weather data was analyzed seasonally to demonstrate the limitation of the static rating approach on ampacity.

For the simulations used in this paper, we chose a 16 km $\times$ 23 km area with an elevation change of over 330 m. Fig. 3 shows the elevation map and locations of the nine weather stations located in this area.

4.1. Test area prevailing winds

Wind flow patterns emerge from horizontal surface and atmospheric temperature contrasts on all spatial scales, from global to local size [48]. Both local and global systems exhibit large regularity of daily and seasonal wind and weather cycles [49]. This regularity can be largely attributed to the local terrain and surface properties. Using year-long data starting July 1, 2012 the prevailing wind direction is illustrated by the wind rose in Fig. 4. Two weather stations ~2 km east of the area investigated were selected because they better represent the boundary conditions of the simulation, therefore used as discussed in Section 3.1.

Because weather stations operate unattended for a long period and adverse weather conditions can exist during winter months, it was necessary to validate the collected data against a common statistical distribution. The distribution of wind speed is commonly defined using the Weibull probability density function [50]. During any time interval the two parameter wind speed probability is given as

$$f(v) = \left(\frac{k}{\lambda}\right)\left(\frac{v}{\lambda}\right)^{k-1} e^{-\left(\frac{v}{\lambda}\right)^{k}} \tag{15}$$

where v is the wind speed, k is the shape parameter, and λ is the scale factor, which is expected to be close to the mean speed. The Weibull probability density function of year-long measured wind

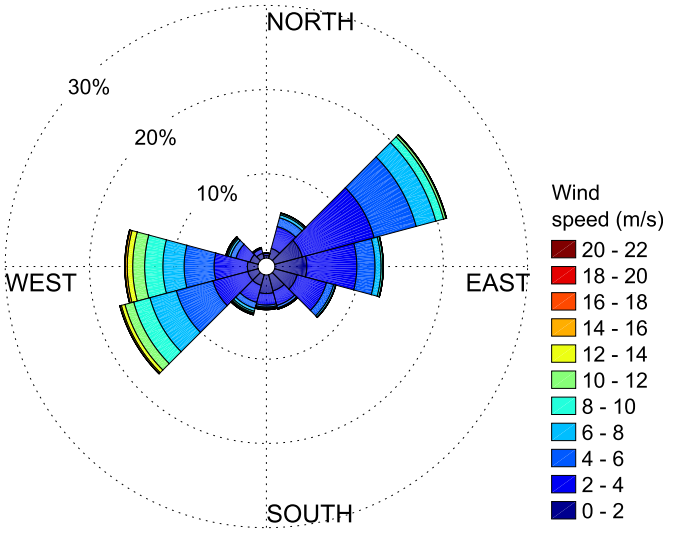

Fig. 4. Wind rose of year-long wind data starting July 1, 2012 from two weather station ~2 km east of the area investigated.

data at each of the weather stations is shown in Fig. 5. The nondimensional shape parameter for the collected data is in agreement with the commonly observed values (i.e. k ranging from 1.6 to 2.4) [50].

5. Results

To demonstrate the feasibility of a simulation-based DLR approach, we first compare our wind solver predictions against field data. A horizontal slice of the eastern region of the target domain in Fig. 3 is the focus of Fig. 6. Eddy sizes vary visibly over the terrain. Long, streak-like structures with low wind speed are evident in the vicinity of the surface. The location of the canyon can be inferred as the flow in to and out of the canyon breaks down the larger eddies vertically above the canyon into much smaller ones. The wind breaks into smaller eddies as it blows over the canyons. Additionally, acceleration of the flow above the canyon can be observed from the color map. We next perform a statistical evaluation of the wind flow simulation.

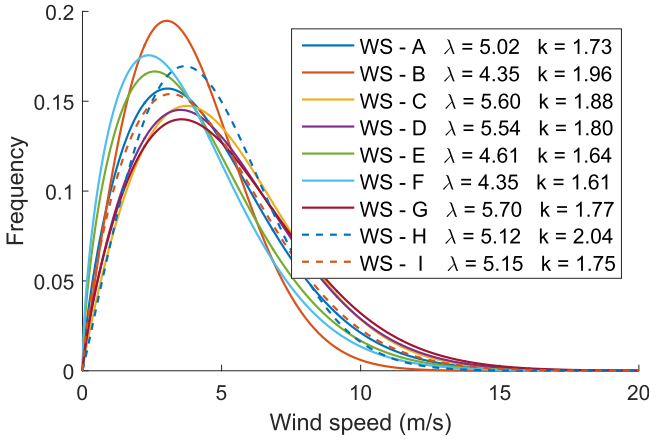

Fig. 5. Weibull wind distribution using year-long wind data from each weather station.

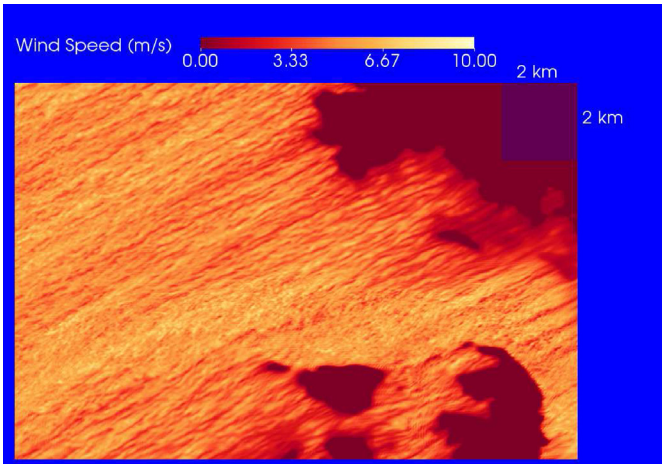

Fig. 6. Flow visualization. Horizontal slice across domain focusing on eastern part of the canyon in the target domain. Flow is from upper-right moving to lower-left. 2 km × 2 km box provided to show scale.

5.1. Statistical validation of the wind solver

To evaluate the wind solver's performance against anemometer data collected at select locations across the test bed area, we follow an approach similar to the one presented in Carvalho et al. [23] by using five statistical parameters: the mean and standard deviation, the root mean squared error (RMSE), the bias, and the standard deviation of the error (STDE). The mean is given as

$$\bar{v} = \frac{1}{N}\sum_{i=1}^{N} v_i \tag{16}$$

where $\bar{v}$ is the mean speed, N is the number of data points, and v_i is the i^{th} wind speed of either the real-time data or simulation results. The standard deviation, S_v, is given as

$$S_v = \sqrt{\frac{1}{N}\sum_{i=1}^{N}(v_i - \bar{v})^2} \tag{17}$$

and the RMSE is computed as

$$RMSE = \left[\frac{1}{N}\sum_{i=1}^{N}(v_i')^2\right]^{1/2} \tag{18}$$

where N is the total number of deviations, v', between the simulated wind speed, v^{sim}, and the respective observed wind speed at the weather station, v^{obs}. The deviation is given as

$$v' = v^{obs} - v^{sim} \tag{19}$$

The bias is defined as

$$Bias = \frac{1}{N}\sum_{i=1}^{N} v_i' \tag{20}$$

and makes possible the evaluation of the data systematic errors. A positive bias means that the simulations overestimate the measured values.

The standard deviation of the error (STDE), helps evaluate the dispersion of the error and it can be written as

$$STDE = \left[RMSE^2 - Bias^2\right]^{1/2}. \tag{21}$$

The STDE removes from the RMSE possible offsets (biases). A low STDE shows if a given error is mainly due to a kind of offset that can more easily be corrected because the underlying physics is correct, whereas a high STDE represents random error and hints unphysical results.

Fig. 7 shows that the mean and standard deviation of the wind speed between the field data and simulation results. We observe that STDE is larger for weather stations B, D and F than the rest of the weather stations. We attribute this difference to the challenges of collecting seasonal data from weather stations that are unattended for long periods. Another issue is that these weather stations were placed to be close to the powerlines and not necessarily at locations that would capture the dominant wind patterns over the area. It is likely that these weather stations are picking up local details that may not be represented in the simulation.

The comparison between field and simulation data is further quantified in Table 3, with an average RMSE value of 0.863, bias of 0.101, and STDE of 0.767. These values are much lower than the values reported in Carvalho et al. [23]. In Michiorri et al. [20] the standard deviation ranged from 0.9 to 1.5, whereas in our approach, it ranges from 0.6 to 1.0. For these reasons, we judge our simulation a reasonable realization of the wind conditions for the assumed global wind direction.

5.2. Dynamic conductor temperature

We perform the transient calculation of the ODE for temperature to demonstrate the dynamic thermal response of the conductor. Eq. (4), using field data from June 10, 2013 at weather station B. Wind speed and ambient temperature values used in the time-marching ODE are updated every 3 min, the rate of field data collection. The initial temperature of the conductor is first solved using the initial wind speed and steady-state equation in the form

$$R(T) = \frac{q_c + q_r - q_s}{I^2} \tag{22}$$

After calculating the resistance, the temperature T is extracted from tabulated data of resistance versus temperature using a linear interpolation. For this hypothetical case, we picked ACSR 26/7 as the conductor type. Static rating was calculated under the summer time assumptions of 0.61 m/s wind, full sun on June 10 at 11AM

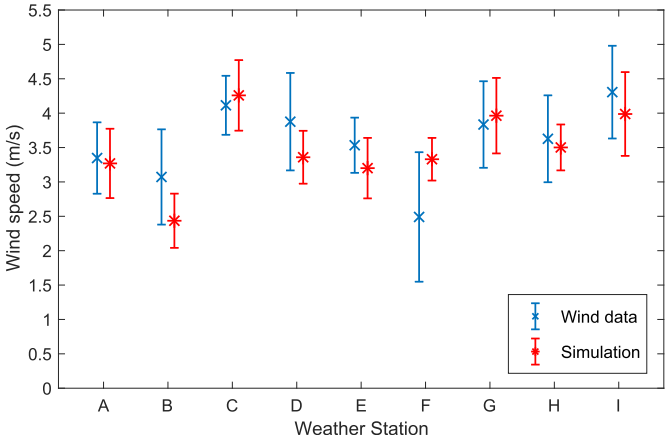

Fig. 7. Mean and standard deviation of the field data and simulation results for wind speed.

Table 3
Statistical comparison between the observed field data and simulated results at each weather station. A negative bias represents a simulated wind speed that is greater than the field data readings.

Weather Station	RMSE (m/s)	Bias (m/s)	STDE (m/s)
A	0.684	0.082	0.679
B	1.047	0.634	0.834
C	0.672	−0.141	0.657
D	0.997	0.526	0.847
E	0.680	0.332	0.591
F	1.295	−0.835	0.990
G	0.855	−0.130	0.846
H	0.762	0.124	0.752
I	0.774	0.318	0.706

(30° latitude, 0 m elevation), and an ambient temperature of 40 °C. Under these assumptions with an allowable maximum conductor temperature of 100 °C, the ampacity was calculated with Eq. (3), giving 1025 Amps. We then imposed a current of 1,025 A to the conductor and calculated the dynamic temperature using the wind speed and ambient temperature field data. Results, presented in Fig. 8, show that conductor temperature—overall—is much lower than the assumed static temperature. Equally important, when adverse conditions persist over long periods of time, TSPs will be informed when conductor temperature is in excess of their limits. Because of these advantages we recommend using a dynamic calculation method over the static rating practice.

As a feasibility test of a simulation-based approach, the conductor temperature was calculated using both field data and simulation results over a 4-h period. Since we are investigating the cooling effect of the wind, we kept other weather conditions constant. The initial conductor temperature used in the ODE calculation was solved using Eq. (22). We updated the wind speed every 3 min and solved the dynamic temperature with a RK4 method over the 4 h. Fig. 9 shows the true mean estimate and highlights the 99% confidence interval (CI). Data from nine weather stations are used to quantify the uncertainty or CI. The true mean estimate, v' is given as

$$v' = \bar{v} \pm CI\ (\%P) \tag{23}$$

where CI is the confidence interval at a given probability, P, and is

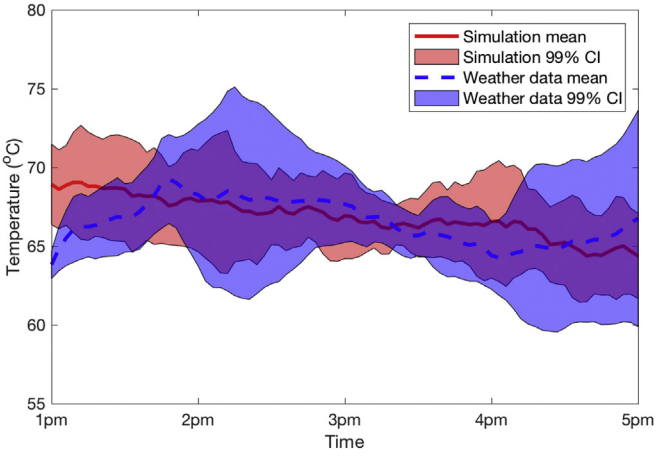

Fig. 9. Resulting conductor temperature using the field data and simulation results. The highlighted area represents the 99% confidence interval.

defined as

$$CI = t_{df,P} \cdot S_{\bar{v}} \tag{24}$$

here $t_{df,P}$ is the statistical t-value with degrees of freedom, df. The degrees of freedom is the number of data points minus one. The standard error, $S_{\bar{v}}$, is defined as

$$S_{\bar{v}} = \frac{S_v}{\sqrt{N}} \tag{25}$$

where S_v is the standard deviation and N is the number of data points.

There are two important conclusions to take away from Fig. 9. First, the conductor temperature is much lower than the 100 °C imposed by the static rating. Second, conductor temperature variation relative to its location is significant as evidenced by the confidence interval. Spatial variation of conductor's temperature justifies the need to resolve the wind field along the length of the line to identify critical segments.

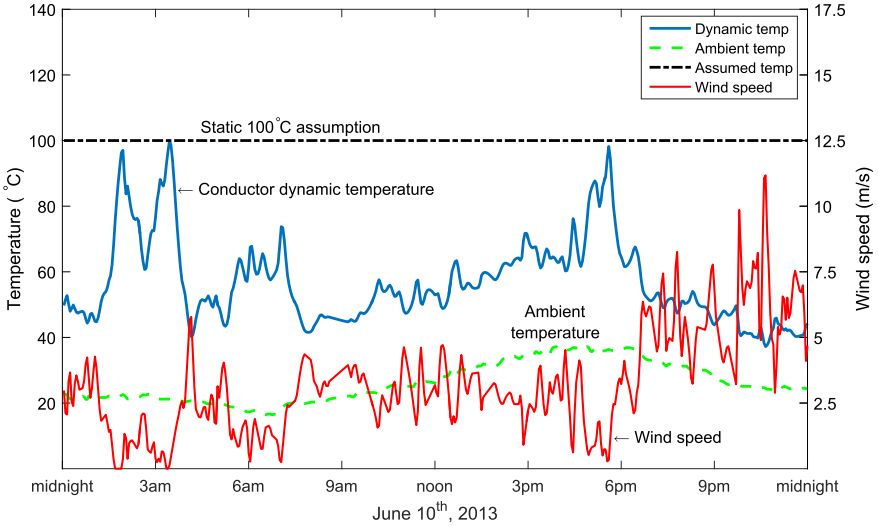

Fig. 8. Conductor dynamic temperature calculated using wind speed and temperature from field data and compared with the assumed 100 °C static temperature when loaded with 1025 Amps.

5.3. Dynamic ampacity

When the conductor is below its maximum allowable temperature, any amount of current can be put on the conductor for a limited amount of time. We therefore calculate the dynamic ampacity using the conductor's present temperature and use an iterative method to solve the current that will heat the conductor to 100 °C in 15 min. To demonstrate this, we show a hypothetical case using ACSR 27/6 conductor with an initial temperature of 60 °C, wind speed of 3.5 m/s, 40 °C ambient temperature, and full sun. The ampacity is calculated to be 1,616 A and the heating can be seen in Fig. 10. If the steady-state thermal rating, Eq. (3), is used under these conditions the ampacity would be at 1,571 A and the conductor response would have to be assumed instantaneous. In other words a dynamic ampacity calculation method would enable the operator to see the actual thermal response of the conductor and its ability to ride out sudden drops in wind speed as it takes some time for the conductor to heat up.

The dynamic ampacity across the test area is therefore calculated using the temperature calculated in section 5.2 and the 15 min transient temperature response to reach 100 °C. The resulting ampacity mean and 99% CI using both field data and simulation results are shown in Fig. 11. The results show that there is significant additional capacity available that is not being utilized.

6. Conclusions

Dynamic line rating (DLR) holds great promise to alleviate transmission congestion that may hinder integration of new power generation. Using actual weather data from measurements and an LES-based micro-scale wind solver, we demonstrated that ampacity of transmission lines in windy areas with complex terrain can be increased by 40–50% through the DLR concept. Our simulation-based approach is non-intrusive for the powerlines, and it is potentially much-more economical than building new transmission lines.

The use of a multi-GPU accelerated solver was critical to the success of our study. Instead of using a commercially available general-purpose computational fluid dynamics solver, we carefully selected our numerical methods and parameterizations to develop a fast wind solver, which was a multi-year effort with multiple developers [32–36]. The hardware-oriented design of our numerical solver —combined with the superior computing power of GPUs— enabled us to accommodate spatial and temporal resolutions that are much finer than the current practice for complex terrain wind simulations. Adoption of fine spatial resolutions is important for the resolution of terrain-induced motions, leading to more accurate line ratings. A potential benefit of using a multi-GPU accelerated solver is that simulations can be performed on workstations or clusters that have a much smaller footprint than central processing unit (CPU) based computing platforms.

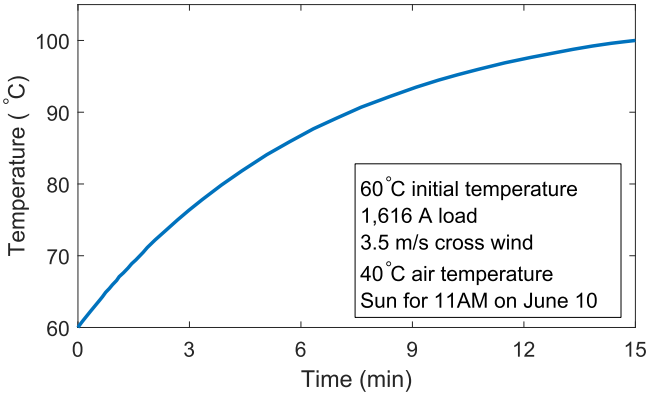

Fig. 10. Conductor heating from 60 to 100 °C in 15 min with a current of 1616 Amps.

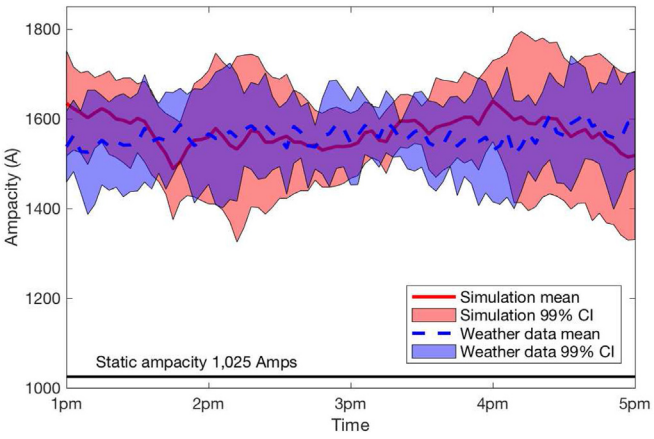

Fig. 11. Resulting dynamic ampacity using field data and simulation results, i.e. this ampacity will heat the conductor from it's present temperature to 100 °C in 15 min. The highlighted area represents the 99% confidence interval.

Statistical analysis of simulation data for wind speed showed a very good agreement with field data. Additionally, we demonstrated that a transient calculation of the conductor temperature offers many advantages over the current practice based on the steady-state response of a conductor. A transient calculation enables us to take advantage of the thermal capacity of a conductor under variable wind conditions when considering a dynamic rating approach. We found that a fourth-order Runge-Kutta scheme performs much better in terms of accuracy and computation time than the forward Euler method suggested in the IEEE-738-2012 standard.

Acknowledgments

This material is based upon work supported by the National Science Foundation under Grant No. 1056110 and 1229709. The second author would like to acknowledge the University of Idaho President's Doctoral Scholars Award. We extend our thanks to Idaho Power for sharing the raw wind data, and helpful discussions with Kurt Meyers and Jake Gentle of Idaho National Laboratory on dynamic line rating concept.

References

[1] Wind Vision: a New Era for Wind Power in the United States, Tech. Rep, U.S. Department of Energy, 2015.
[2] D. of Energy, 20% Wind Energy by 2030: Increasing Wind Energy's Contribution to U.S. Electricity Supply, Technical Report DOE/GO-102008–2567, 2008.
[3] A. Arroyo, P. Castro, R. Martinez, M. Manana, A. Madrazo, R. Lecuna, A. Gonzalez, Comparison between IEEE and CIGRE thermal behaviour standards and measured temperature on a 132-kv overhead power line, MDPI Energ. 8 (2015) 13660–13671.
[4] J. Metevosyan, Wind power in areas with limited transmission capacity, in: T. Ackermann (Ed.), Wind Power in Power Systems, John Wiley and Sons, 2005, pp. 433–501. Ch. 20.
[5] R.S. Jorge, E.G. Hertwich, Environmental evaluation of power transmission in Norway, Elsevier Appl. Energy 101 (2013) 513–520.
[6] J. Hall, A. Deb, Prediction of overhead transmission line ampacity by stochastic and deterministic models, IEEE Power Deliv. 3 (2) (1988) 789–800.
[7] J. Reding, A method for determining probability based allowable current ratings for BPA's transmission lines, IEEE Power Deliv. 9 (1) (1994) 153–161.
[8] P. Pytlak, P. Musilek, E. Lozowski, J. Toth, Modelling precipitation cooling of overhead conductors, Elsevier Electr. Power Syst. Res. 81 (12) (2011) 2147–2154.

[9] J. Cho, J. Kim, J. Lee, J. Kim, I. Song, J. Choi, Development and improvement of an intelligent cable monitoring system for underground distribution networks using distributed temperature sensing, MDPI Energ. 7 (2) (2014) 1076–1094.
[10] C. Holyk, H.D. Liess, S. Grondel, H. Kanbach, F. Loos, Simulation and measurement of the steady-state temperature in multi-core cables, Elsevier Electr. Power Syst. Res. 116 (2014) 54–66.
[11] J. Hosek, Dynamic thermal rating of power transmission lines and renewable resources, in: ES1002 Workshop, Paris, France, 2011, pp. 1–3.
[12] J. Heckenbergerova, J. Hosek, Dynamic thermal rating of power transmission lines related to wind energy integration, in: Environment and Electrical Engineering (EEEIC), 2012 11th International Conference on, 2012, pp. 798–801.
[13] E. Fernandez, I. Albizu, M. Bedialauneta, A. Mazon, P. Leite, Review of dynamic line rating systems for wind power integration, Renew. Sustain. Energy Rev. 53 (2016) 80–92.
[14] S. Uski-Joutsenvuo, R. Pasonen, S. Rissanen, Maximising Power Line Transmission Capability by Employing Dynamic Line Ratings: Technical Survey and Applicability in Finland, Research Report, VTT-R-01604–13, 2013.
[15] EPRI, Increased Power Flow Guidebook: Increasing Power Flow in Transmission and Substation Circuits, Palo Alto, CA. 1010627, 2005.
[16] T.O. Seppa, A practical approach for increasing the thermal capabilities of transmission lines, IEEE Trans. Power Deliv. 8 (3) (1993) 1536–1550.
[17] T.O. Seppa, R.D. Mohr, J. Stovall, Error Sources of Real-time Ratings Based on Conductor Temperature Measurements, Report to CIGRE WG B2.36, 2010, pp. 20–21.
[18] J. Gentle, K.S. Myers, T. Baldwin, I. West, K. Hart, B. Savage, M. Ellis, P. Anderson, Concurrent wind cooling in power transmission lines, in: 2012 Western Energy Policy Research Conference, 2012. INL/CON-12–27012.
[19] D.M. Greenwood, J.P. Gentle, K.S. Myers, P.J. Davison, I.J. West, J.W. Bush, G.L. Ingram, M.C. Troffaes, A comparison of real time thermal rating systems in the U.S. and the U.K, IEEE Trans. Power Deliv., 29 (4).
[20] A. Michiorri, P.C. Taylor, S.C.E. Jupe, Overhead line real-time rating estimation algorithm: description and validation, Proc. Institut. Mech. Eng. Part A J. Power Energy 224 (3) (2010) 293–304.
[21] A. Michiorri, H.-M. Nguyen, S. Alessandrini, J.B. Bremnes, S. Dierer, E. Ferrero, B.-E. Nygaard, P. Pinson, N. Thomaidis, S. Uski, Forecasting for dynamic line rating, Renew. Sustain. Energy Rev. 52 (2015) 1713–1730.
[22] M.G.-G. David Carvalho, Alfred Rocha, C. Santos, WRF wind simulation and wind energy production estimates forced by different reanalyses: comparison with observed data for Portugal, Appl. Energy 117 (2014) 116–126.
[23] M.G. David Carvalho, Alfred Rocha, C. Santos, A sensitivity study of the WRF model in wind simulation for an area of high wind energy, Elsevier Environ. Model. Softw. 33 (2012) 23–34.
[24] M. Bhaskar, A. Jain, N.V. Srinath, Wind speed forecasting: present status, in: Power System Technology (POWERCON), 2010 International Conference, 2010, pp. 1–6.
[25] M. Negnevitsky, P. Mandal, A. Srivastava, An overview of forecasting problems and techniques in power systems, in: Power Energy Society General Meeting, 2009. PES 2009, IEEE, 2009, pp. 1–4.
[26] S. Soman, H. Zareipour, O. Malik, P. Mandal, A review of wind power and wind speed forcasting methods with different time horizons, in: North American Power Symposium (NAPS), 2010, pp. 1–8.
[27] B. Banerjee, D. Jayaweera, S. Islam, Risk constrained short-term scheduling with dynamic line ratings for increased penetration of wind power, Renew. Energy 83 (2015) 1139–1146.
[28] IEEE, IEEE standard 738–2012: IEEE standard for calculating the current-temperature relationship of bare overhead conductors.
[29] CIGRE, The thermal behaviour of overhead conductors, CIGRE WG 12.
[30] CIGRE Working Group B2.12, Guide for Selection of Weather Parameters for Bare Overhead Conductor Ratings, Tech. Rep. 299, August 2006.
[31] S.C. Chapra, R.P. Canale, Numerical Methods for Engineers, sixth ed., McGraw Hill, Boston, MA, 2010.
[32] J.C. Thibault, I. Senocak, Accelerating incompressible flow computations with a Pthreads-CUDA implementation on small-footprint multi-GPU platforms, J. Supercomput. 59 (2) (2012) 693–719.
[33] D.A. Jacobsen, I. Senocak, Multi-level parallelism for incompressible flow computations on GPU clusters, Parallel Comput. 39 (1) (2013) 1–20, http://dx.doi.org/10.1016/j.parco.2012.10.002.
[34] D.A. Jacobsen, I. Senocak, A full-depth amalgamated parallel 3D geometric multigrid solver for GPU clusters, in: 49th AIAA Aerospace Science Meeting, No. AIAA-2011-946, 2011. Orlando, FL.
[35] R. DeLeon, K. Felzien, I. Senocak, Toward a GPU-accelerated immersed boundary method for wind forecasting over complex terrain, in: Proceedings of the ASME 2012 Fluids Engineering Division Summer Meeting, 2012 no. FEDSM2012–72145.
[36] R. DeLeon, D. Jacobsen, I. Senocak, Large-eddy simulations of turbulent incompressible flows on GPU clusters, Comput. Sci. Eng. 15 (1) (2013) 26–33.
[37] I. Senocak, A. Ackerman, M. Kirkpatrick, D. Stevens, N. Mansour, Study of near-surface models for large-eddy simulations of a neutrally stratified atmospheric boundary layer, Boundary-Layer Meteorol. 124 (2007) 405–424.
[38] C. Meneveau, T. Lund, W. Cabot, A lagrangian dynamic subgrid-scale model of turbulence, J. Fluid Mech. 319 (1996) 353–385.
[39] L. Prandtl, Bericht über die Entsteung der Turbulenz, X, Angew. Math. Mech. 5 (1925) 136–139.
[40] I. Senocak, A. Ackerman, D. Stevens, N. Mansour, Topography modeling in atmospheric flows using the immersed boundary method, in: Annual Research Briefs, Center for Turbulence Research, NASA-Ames/Stanford Univ., Palo Alto, CA, 2004, pp. 331–341.
[41] J. Mohd-Yusof, Combined immersed boundary/B-spline methods for simulations of flow in complex geometries, in: Annual Research Briefs, Center for Turbulence Research, NASA-Ames/Stanford University, 1997.
[42] R. Verzicco, J. Mohd-Yusof, P. Orlandi, D. Haworth, Large eddy simulation in complex geometric configurations using boundary body forces, AIAA J. 38 (2000) 427–433.
[43] I. Senocak, M. Sandusky, R. DeLeon, D. Wade, K. Felzien, M. Budnikova, An immersed boundary geometric preprocessor for arbitrarily complex terrain and geometry, J. Atmos. Ocean. Tech. 32 (11) (2015) 2075–2087.
[44] R.B. Stull, An Introduction to Boundary Layer Meteorology, Kluwer Academic Publishers, Dordrecht, Netherlands, 1988.
[45] Renewable NRG Systems, Hinesburg, Vermont, NRG 40C Anemometer, March 2015.
[46] APRS World, LLC, Winona, MN, APRS #40R (2015).
[47] T. Phillips, I. Senocak, J. Gentle, K. Myers, P. Anderson, Investigation of a dynamic power line rating concept for improved wind energy integration over complex terrain, in: Proceedings of the ASME 2014 4th Joint US-European Fluids Engineering Division Summer Meeting, 2014 no. FEDSM2014–21377.
[48] S. Emeis, Wind Energy Meteorology: Atmospheric Physics for Wind Power Generation, Springer, Verlag Berlin Heidelberg, 2013.
[49] A.K. Deb, Powerline Ampacity System; Theory, Modeling, and Applications, CRC Press, Boca Raton London New York Washington, D.C, 2000.
[50] M. Brower (Ed.), Wind Resource Assessment: a Practical Guide to Developing a Wind Project, John Wiley & Sons, Hoboken, NJ, 2012.